

Characterization of nanopore morphology of shale and its effects on gas permeability



Jiangtao Zheng^{a, b}, Ziyang Wang^a, Wenbo Gong^b, Yang Ju^{b, c}, Moran Wang^{a, *}

^a Department of Engineering Mechanics, School of Aerospace, Tsinghua University, Beijing 100084, China

^b State Key Laboratory of Coal Resources and Safe Mining, China University of Mining & Technology at Beijing, Beijing 100083, China

^c State Key Laboratory for Geomechanics and Deep Underground Engineering, China University of Mining & Technology, Xuzhou 221006, China

ARTICLE INFO

Article history:

Received 20 March 2017

Received in revised form

30 August 2017

Accepted 7 October 2017

Available online 12 October 2017

Keywords:

Shale gas

FIB-SEM

Pore morphology

High-Knudsen effect

LBM simulation

ABSTRACT

From a microscopic point of view, nano-scale pores are dominant in shale matrix, which provide transport space for natural gas. Accordingly, a pore-scale modeling, which can accurately capture the complex pore morphology and its effects on gas flow behavior, is crucial for understanding the gas transport mechanisms in shale matrix. In this study, the focused ion beam-scanning electron microscope (FIB-SEM) technique was employed to observe and characterize the morphology of the nanopores in shale. Based on the morphology characterizations, three representative porous models (i.e. intergranular pore model, micro-crack model and “honeycomb” pore model) were proposed and generated by numerical methods. The high-Knudsen gas flows in these generated structures were simulated by the lattice Boltzmann method (LBM). A comparison of the simulation results among these three porous models suggests that the nano-scale pore morphology plays an important role in the gas transport properties. Moreover, the high-Knudsen effect leads to a larger apparent permeability for each nano-scale porous model. Our work indicates the importance of the nano-scale pore morphology and the high-Knudsen effect on gas transport properties of shale matrix.

© 2017 Elsevier B.V. All rights reserved.

1. Introduction

Natural gas extraction from deep underground shale formations (shale gas) gained worldwide attention since profitable extraction was achieved in North America (Liang et al., 2014). Shale gas reservoirs are usually referred to as “unconventional reservoirs” due to the micro-to nanometer sized pore spaces and the lack of economical production ability before reservoir stimulation (Jackson et al., 2014). Generally, horizontal drilling and hydraulic fracturing are employed to increase the effective transport channels for the gas flow toward the wellbore. However, despite these treatments, only a small fraction (approximately 5–30%) of shale gas can be extracted (Bažant et al., 2014). This is mainly attributed to the extremely restricted transport property of shale matrix situated between the artificially created hydraulic fractures. A better understanding of the transport mechanisms, which govern the gas flow behavior within the porous structure of shale matrix, is thus important for developing an optimal exploitation method (Zheng

et al., 2016).

In order to gain a deeper understanding of the macroscopic shale matrix transport properties, it is indispensable to obtain insights from the microscopic gas flow behavior in its nano-scale porous structure (Heller et al., 2014; Gensterblum et al., 2015). An accurate description of porous structures in shale matrix is needed in the first place. Advanced imaging methods, such as nanoscale X-ray computed tomography (nano-CT) (Akbarabadi and Piri, 2014) and focused ion beam-scanning electron microscope (FIB-SEM) (Kelly et al., 2016; Bultreys et al., 2016), are now available to observe the nano-scale porous structures in shale. With these methods, three-dimensional (3D) porous structures in shales from different regions were depicted (Kelly et al., 2016; Klaver et al., 2015; Loucks et al., 2012; Chalmers et al., 2012). These results combined with the pore size distribution tests (Chalmers et al., 2012) show that nano-scale pores are dominant in an intact shale sample. Besides, the porous structures in shale are very complex, which result from multiple mineral compositions, diagenetic processes and hydrocarbon generation processes. Statistically, the porous structures are anisotropic and heterogeneous (Wang et al., 2016a). Moreover, from a morphological point of view the porous

* Corresponding author.

E-mail address: mrwang@tsinghua.edu.cn (M. Wang).

structures are quite diverse and vary from “honeycomb” like pores in organic matter, intergranular irregular shaped pores and hydrocarbon generation related micro-cracks (Loucks et al., 2012). Accordingly, pore-scale models which can accurately represent these complex pore morphologies are crucial for understanding the related gas transport mechanisms. As noted by previous studies (Wang et al., 2010; Wang and Pan, 2008; Ju et al., 2013, 2014), the morphology of different types of porous structures influence the effective properties of porous media. However, little attention has been focused on the influence of nano-scale pore morphology on the gas permeability.

As the flows in shale matrix are confined in nano-scale pores, the conventional Darcy's law, which assumes a non-slip boundary condition, is not always applicable under reservoir conditions (Fink et al., 2017; Javadpour et al., 2007; Lauga et al., 2007). For such gas flows, the Knudsen number (Kn), which is defined as the ratio between the mean free path (λ) and the characteristic length (l) of the flow region, is relatively large ($Kn > 0.001$) and the continuum assumption breaks down (Wang and Li, 2003; Wang et al., 2008; Guo et al., 2008; Aidun and Clausen, 2010; Li et al., 2011). Hence, the contribution of gas slip on the solid boundary cannot be ignored (Wang et al., 2008; Guo et al., 2008; Chai et al., 2011; Cho et al., 2013; Wang and Yin, 2017; Wu and Struchtrup, 2017; Suga et al., 2010) and the obtained apparent permeability (k_a) is larger than the intrinsic permeability (k_0). This was first experimentally proven by Klinkenberg (1941) and followed by several analytical and numerical models that proposed solutions to capture the high- Kn effect. For instance, Ohwada et al. (1989), studied the high- Kn gas flow on the basis of a linearized Boltzmann equation. Beskok and Karniadakis (1999) reported a semi-analytical model for high- Kn gas flow in the straight channel and pipe geometries. Civan (2010) extended the equation for gaseous flow through tight porous media. Kalarakis et al. (2012), simulated the gas flow in channels and reconstructed porous media using a direct simulation Monte Carlo (DSMC) method and a modified LBM. Their results suggested that k_a increases two orders as the Kn increased from 0.1 to 10.

For high- Kn flow simulation, LBM has higher computational efficiency compared to DSMC, which makes it suitable for studying the flow in complex porous structures (Chai et al., 2011; Cho et al., 2013; Wang and Yin, 2017; Wu and Struchtrup, 2017). Guo et al. (2008), proposed a generalized lattice Boltzmann equation with multiple effective relaxation times for the unidirectional high- Kn gas flow. Li et al. (2011), simulated microchannel flows in the transition flow regime using LBM and the results agreed well with the linearized Boltzmann equation, the DSMC, and the experimental results. Wang et al. (Wang and Yin, 2017), simulated the gas flow with surface slip in 3D geometries composed of different arrays of spheres. Recently, Wang et al. (2016a, 2016b), employed LBM in simulating in-situ shale gas flow and investigated the influence of statistical geometry effects on gas permeability. As indicated by previous studies, LBM can accurately account for high- Kn gas flows in complex porous structures, which makes it a popular tool for studying the flow behavior in the shale matrix.

In this study, we investigated the nano-scale pore morphology within a shale matrix and its influence on high- Kn gas transport. At first, the microscopic porous structures of shale were observed and characterized by FIB-SEM imaging. Based on the morphology characterizations, three representative types of porous models were proposed and numerically generated. Finally, the high- Kn gas flow was simulated by LBM, in order to obtain the k_0 and k_a of the three porous models. The influences of pore morphology on shale matrix permeability were discussed based on the calculations.

2. Characterization and reproduction of porous structure in shale

It is known that complex nano-scale pores are dominant in shale matrix according to recent publications (Kelly et al., 2016; Klaver et al., 2015; Loucks et al., 2012; Chalmers et al., 2012). The morphology of these nano-scale pores exhibits diverse characteristics, which contribute differently to the transport properties. In this work, the porous structures in shale were observed by FIB-SEM. According to the pore morphology features, three typical structural models were proposed. For each model, a numerical reconstruction method was employed to generate representative porous structures.

2.1. Pore morphology characterization

FIB-SEM was used to investigate 3D porous structures in shale samples drilled from an outcrop of Lower Silurian Longmaxi formation, Sichuan Basin, China. The formation (Ju et al., 2017a) has a high total organic carbon content of 2.28% and a high thermal maturity of $Ro = 2.11\%$. Three sets of FIB-SEM observations were conducted which intentionally focused on different porous regions of the shale samples. The FIB-SEM image resolution of each observation was chosen to provide a clear indication of the porous structures. Two sets focused on interparticle regions with trench sizes of $22 \times 15 \mu\text{m}$ and $16 \times 14 \mu\text{m}$ and image resolutions of 22 nm and 15 nm, respectively. A third set focused on the organic matter region with a trench size of $13 \times 11 \mu\text{m}$ and an image resolution of 6 nm. The milled thickness by the FIB each time was 10 nm for all the three sets.

These image sets obtained by FIB-SEM provide useful information to classify different pore morphologies in shale, with respect to the pore shape, position and surrounding mineral compositions. Three representative image cuts of the three observations are shown in Fig. 1. Based on these observations, three typical pore morphology models were defined: intergranular pore model, micro-crack model and “honeycomb” pore model. As illustrated in Fig. 1(a), irregular shaped intergranular pores mainly appeared between particles. The formation of these intergranular pores is related to the compaction of particles. The micro-cracks, which may be related to the hydrocarbon generation process, are shown in Fig. 1(b). These micro-cracks usually appeared near organic matter and around edges of some hard mineral particles. The pores in the organic matter result from hydrocarbon generation processes and have a shape similar to a “honeycomb”, as shown in Fig. 1(c). In high matured shales, as the one shown in Fig. 1(c), the “honeycomb” pores usually occupy a large portion of the organic matter.

2.2. Porous structure generation

In order to give a quantitative description of the influence of the nano-scale pore morphology on the gas transport properties, 150 of porous models were generated by numerical reconstruction methods based on the pore morphology characterization. The generated 3D digital structures were composed of black and white voxels representing pore space and rock matrix, respectively. Each structure has a size of $64 \times 64 \times 64$ voxels.

The porosity (ϕ) of each reconstructed structure is defined as the number of black voxels divided by the total voxel number. Moreover, the effective porosity (ϕ_e) is defined by solely taking into account the connected voxels on the flow direction X. In the calculation of ϕ_e , all pore voxels were firstly labeled with the connected ones labeled as the same value. Thereafter, the number of connected pore voxels from the surface of $X = 1$ to the surface of $X = 64$ was calculated and utilized to calculate ϕ_e .

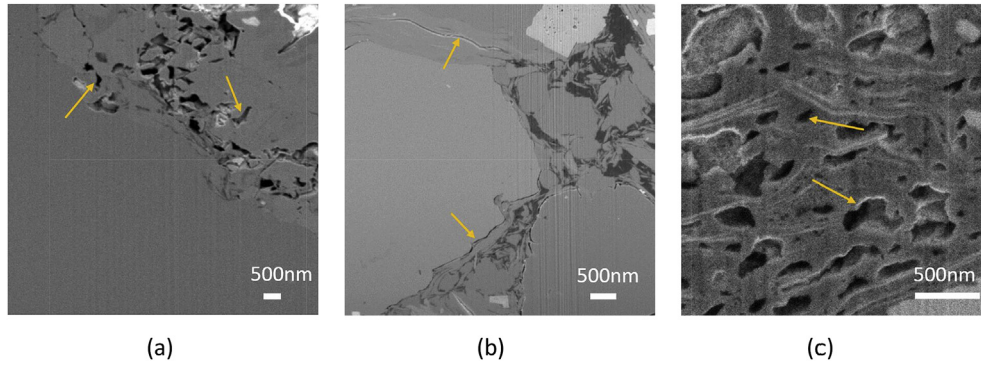


Fig. 1. Representative porous structures in shale matrix observed by FIB-SEM with image size of 400×400 voxels. (a) Intergranular pores with voxel resolution of 22nm, (b) micro-crack with voxel resolution of 15nm and (c) organic pores with voxel resolution of 6nm.

2.2.1. Representing of intergranular pore model

A random sphere packing method (Ju et al., 2017b) was used to generate the intergranular pore models. In this procedure, white spheres were randomly inserted into a predefined black cubic box with a side length of 64 voxels until the porosity equaled to the predefined value. A uniform sphere with a radius equal to 4 voxels was used in the generation process and they were allowed to overlap with each other. Five sets of the intergranular pore model were generated with porosities equal to 8%, 10%, 12%, 14% and 16%, respectively. In each porosity set, 10 random structures were generated to give a statistical quantification. A 3D appearance of the generated intergranular pore structure with 10% porosity is shown in Fig. 2(a) and the center slice perpendicular to X direction is shown in Fig. 2(b).

2.2.2. Representing of micro-crack model

A random crack generation method was proposed to generate micro-crack models. In the procedure, random crack planes were sequentially cast into a predefined white cubic box with a side length of 64 voxels until the porosity equaled to a predefined value. Similarly, five sets of micro-crack model were generated with porosities of 8%, 10%, 12%, 14% and 16%, respectively, and each set contained ten random structures. In the model, each crack plane was defined by a random point (x_0, y_0, z_0) and a random vector (a, b, c) . The value of x_0, y_0 and z_0 were random integers from 1 to 64. The

value of a, b and c were random integers from -64 to 64. In the casting process, the voxels with a coordinator of (x, y, z) , which met the criterion defined by the following Eq. (1), were chosen as the crack voxels:

$$\frac{\text{abs}(a \times (x - x_0) + b \times (y - y_0) + c \times (z - z_0))}{\sqrt{a^2 + b^2 + c^2}} \leq 1 \quad (1)$$

Under this setting, the effective aperture of each crack was 3 voxels. A 3D appearance of the generated micro-crack model with 10% porosity is shown in Fig. 3(a) and the center slice perpendicular to X direction is shown in Fig. 3(b).

2.2.3. Representing of honeycomb pore model

A similar random sphere packing method was employed to generate honeycomb pore models. The difference is that black spheres, i.e. pore voxels, were randomly put into a predefined white cubic box with a side length of 64 voxels. A uniform sphere with a radius of 4 voxels was used in the generation. Predefined porosities for the five sets were 30%, 35%, 40%, 45% and 50%, respectively. Again, each set contained ten random structures. The high porosity is in consistent with the cases of high mature organic matter in shale, as shown in Fig. 1(c). A 3D appearance of a generated honeycomb pore model with 40% porosity is shown in Fig. 4(a) and the center slice perpendicular to X direction is shown in Fig. 4(b).

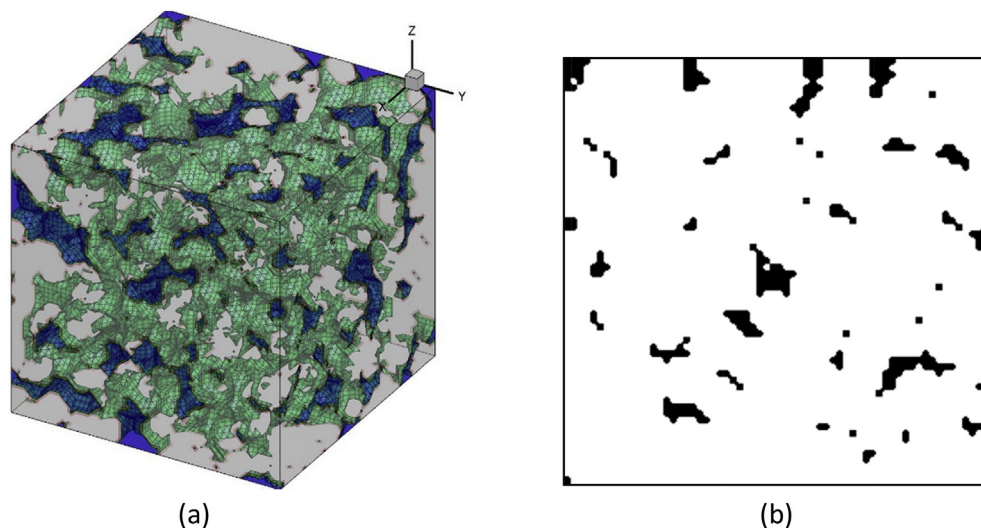


Fig. 2. Illustration of the generated intergranular pore model. (a) 3D appearance of the model, (b) center slice perpendicular to X direction.

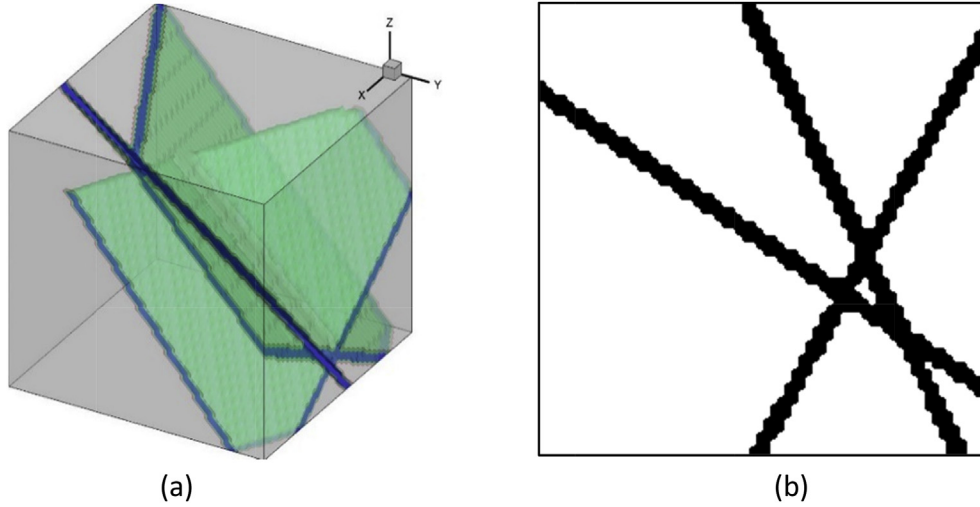


Fig. 3. Illustration of the generated micro-crack model. (a) 3D appearance of the model, (b) center slice perpendicular to X direction.

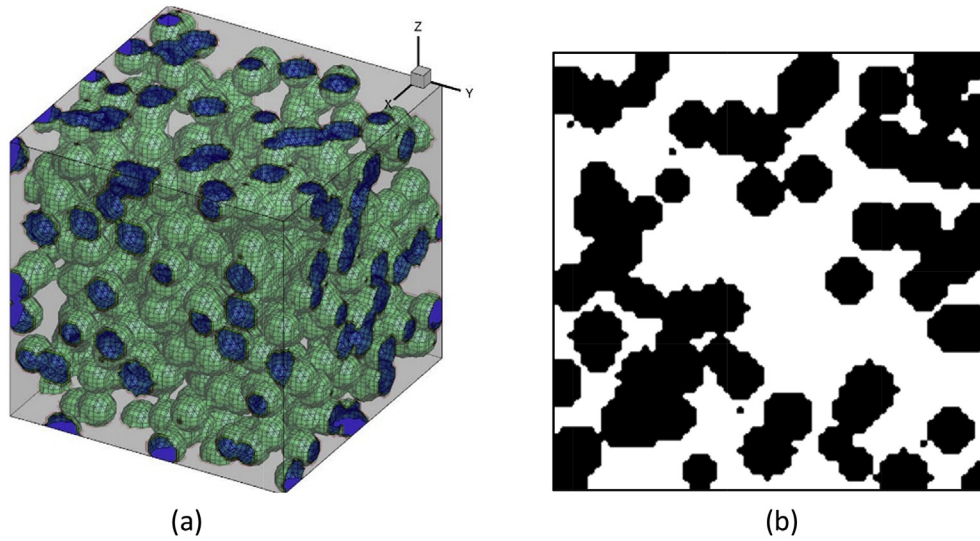


Fig. 4. Illustration of the generated honeycomb pore model. (a) 3D appearance of the model, (b) center slice perpendicular to X direction.

3. LBM for gas flows in nanopores

3.1. Basic lattice Boltzmann equation

The LBM is employed for simulating high- Kn gaseous flows in the reconstructed porous structures due to the following two reasons: (1) it is directly derived by discretization of the Boltzmann equation (Chen and Gary, 1998; He and Luo, 1997), which is the fundamental transport equation for high- Kn flow; (2) it is convenient and efficient in dealing with complex boundaries of porous structure (Sukop and Thorne, 2006). A detailed review of applying LBM in micro-gaseous flow can be found in Wang et al. (2016c). In general, the lattice Boltzmann equation without a body force term is written as:

$$f_i(\mathbf{x} + \mathbf{c}_i \Delta t, t + \Delta t) - f_i(\mathbf{x}, t) = \Omega_i(f_i) \quad (2)$$

where $f_i(\mathbf{x}, t)$ is the discrete density distribution function at location \mathbf{x} and time t , \mathbf{c}_i is the lattice speed, $\Omega_i(f_i)$ is the collision operator. In this work, the 3-dimensional 19-speed (D3Q19) model and

multiple relaxation time (MRT) collision operator are employed to ensure the simulation accuracy and stability (d'Humières, 2002). The MRT collision operator is:

$$\Omega_i(f_i) = - \sum_j (\mathbf{M}^{-1} \mathbf{S} \mathbf{M})_{ij} (f_j - f_j^{\text{eq}}) \quad (3)$$

where f_j^{eq} is the equilibrium distribution function. \mathbf{M} is a 19×19 transformation matrix, which maps the distribution functions onto the moment space (d'Humières, 2002). \mathbf{S} is a diagonal matrix and its value employed in this work is according to Pan et al. (2006):

$$\mathbf{S} = \text{diag}(0, s_e, s_e, 0, s_q, 0, s_q, 0, s_q, s_\nu, s_\pi, s_\nu, s_\pi, s_\nu, s_\nu, s_m, s_m, s_m) \quad (4)$$

where $s_\nu = \frac{1}{\tau}$ and $s_e = s_\varepsilon = s_q = s_\pi = s_m = 8 \frac{2-s_\nu}{8-s_\nu}$, τ is the relaxation time which is related to the macroscopic kinetic viscosity as $\nu = \frac{dx^2}{3dt} (\tau - 0.5)$. The macroscopic physical density and velocity of the flow is computed by the distribution function as:

$$\rho = \sum_i f_i, \quad \mathbf{u} = \sum_i \mathbf{c}_i f_i \quad (5)$$

3.2. LBM for high-Kn flow

In order to accurately simulate the high-Kn flow by LBM, a similar procedure as proposed by (Wang et al., 2016a, 2016b; Guo et al., 2008; Li et al., 2011) was employed in this work. Especially, two property changes of high-Kn flow were considered in the simulation: 1) gas slip on the wall boundary and 2) a lower effective viscosity.

Kn is defined as:

$$Kn = \frac{\lambda}{l} \quad (6)$$

where λ is the mean free path of gas and l is the characteristic length of the pores in the model. For the micro-crack model, l is defined as the aperture of the micro-crack, which equals to 3 lattice length. The l for the intergranular pore model and the honeycomb pore model are defined by the well-known Kozeny-Carman (K-C) model (Carman, 1997):

$$l = \frac{2V_p}{S_p} \quad (7)$$

where V_p is the pore volume and S_p is the surface area of the pore space. The l defined by this method gives an accurate description of average pore size and simplifies the following calculation. Additionally, the simulated gas in this work was treated as methane due to the fact that the main component of shale gas is methane (Loucks et al., 2012). The mean free path of the gas is calculated by:

$$\lambda = \frac{\mu}{\rho} \sqrt{\frac{\pi M}{2RT}} \quad (8)$$

where μ is gas viscosity, ρ is gas density, M is gas molar mass, R is gas constant which equals to 8.314 (J·mol⁻¹/K) and T is temperature.

The fully diffusive boundary condition (Ansumali and Karlin, 2002) is implemented as:

$$f_i^{\text{new}} = \omega_i \frac{\sum_{j, \text{solid}} f_j}{\sum_{j, \text{solid}} \omega_j} \quad (9)$$

where $\sum_j f_j$ represents the sum of f_j which toward a solid node. f_i^{new} are the diffused outgoing distribution functions on the solid node. In the next streaming step, the f_i^{new} propagate to the nearby fluid nodes. Moreover, the Bosanquet-type effective viscosity is calculated by:

$$\mu_e = \frac{\mu}{1 + aKn} \quad (10)$$

where a is an empirical parameter equaling to 2.2 (Beskok and Karniadakis, 1999).

To validate the simulation method, micro-gaseous flows in a straight channel under different conditions were simulated. The channel length and height were 500 nm and 55 nm respectively, in a calculation domain of 100 × 13 lattices. A small pressure gradient was applied in the simulation using the non-equilibrium extrapolation method (Guo et al., 2002).

At first, the intrinsic permeability (k_0) of the channel was

calculated at different values of τ without considering the high-Kn effect. In this case, the bounce-back boundary condition and the intrinsic gas viscosity were used in the calculation. It should be noted that under such conditions k_0 is only a property of the channel height H , i.e., $k_0 = H^2/12$. The MRT scheme showed more stable and accurate results compared to the single relaxation time (SRT) scheme. As shown in Fig. 5(a), the k_0 results calculated by the MRT scheme are almost the same as theoretical values for a wide range of τ . However, the SRT scheme is applicable only for small values of τ . The stability of the MRT scheme for different values of τ is crucial for the accurate simulation of high-Kn gas flow.

Secondly, high-Kn gas flow ($Kn = 0.709$) in the same channel was simulated by the MRT scheme, using diffusive wall boundary and effective viscosity. The velocity profile agrees well with the model proposed by Beskok and Karniadakis (1999), as shown in Fig. 5(b). These results demonstrate the capability of our method in simulating the high-Kn gas flows.

4. Simulation of flow in different pore morphologies

The validated LBM was employed to investigate the micro-gaseous flow in the three typical porous models. The parameters listed in Table 1 were used to simulate the gas flow in the porous structures as generated in Section 2. The k_0 of each generated structure was calculated with non-slip boundary condition and intrinsic viscosity. The k_a was obtained by high-Kn gas flow simulation. In the simulations, a small pressure gradient along X direction was applied using the non-equilibrium extrapolation method (Guo et al., 2002). The average velocity in the flow direction (\bar{U}_x) was monitored at each iteration time step. The iteration process stopped when the velocity nearly unchanged: $\left| \frac{\bar{U}_x - \bar{U}_x'}{\bar{U}_x} \right| < 10^{-5}$, where \bar{U}_x' is the average velocity in the previous iteration time step. Subsequently, the permeability was calculated based on the velocity data.

4.1. Micro-gaseous flow in intergranular pore model

k_0 and k_a of the intergranular pore model were calculated by the proposed method. For each porosity set, ten randomly generated structures were analyzed. The average ϕ_e for each porosity set is given in Table 2. When $\phi > 10\%$, the value of ϕ_e is close to ϕ . However, the value of ϕ_e is significantly less than ϕ when $\phi \leq 10\%$. The average Kn under the simulation settings is also listed in Table 2.

In the simulation, two parallel computations were performed for obtaining the k_0 and k_a of each structure. Comparisons of k_0 and k_a at different porosities are shown in Fig. 6. As shown, the permeability increases about one order as the porosity doubled from 8% to 16%. Moreover, k_a is more than two times larger than k_0 at the same porosity, indicating that high-Kn effect is significant.

4.2. Micro-gaseous flow in micro-crack model

Ten micro-crack structures were generated for each of the five porosity sets with an effective crack aperture of 3 lattice length. The crack length is allowed long enough to cross through the cubic domain. As a result, ϕ_e of each set is almost equal to ϕ . For the given parameter settings in Table 1, Kn for each micro-crack structure equals 0.173.

Two parallel computations were performed to obtain the k_a and k_0 of each micro-crack structure. As presented in Fig. 7, k_a and k_0 approximately show a positive linear correlation with the porosity increase, which is reasonable as the number of cracks in the system increases linearly with the total porosity as well. In addition, the average k_a is about two times larger than k_0 for each porosity set.

Compared with the intergranular pore model, micro-crack

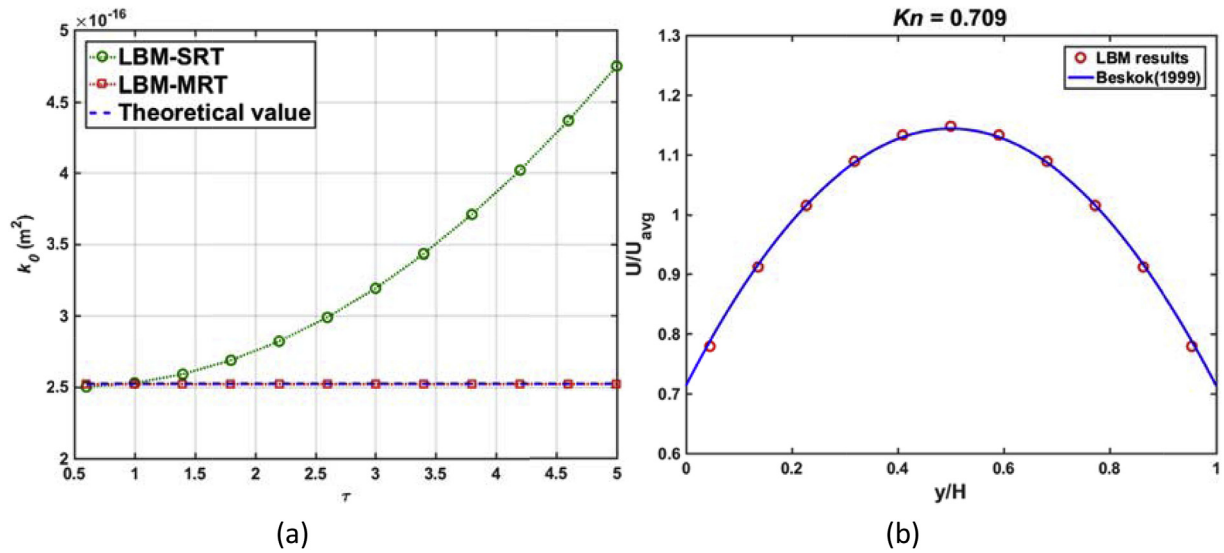


Fig. 5. Validations of micro-gaseous flow simulation. (a) Comparison of the accuracy of MRT and SRT scheme. (b) The velocity profile of high- Kn gas flow in a single nano-channel.

Table 1

Parameters used in the high- Kn gas flow simulation.

Domain size (lattices)	$64 \times 64 \times 64$
Lattice length, dx (m)	5×10^{-9}
Temperature, T (K)	380
Gas constant, R ($\text{J} \cdot \text{mol}^{-1} \cdot \text{K}^{-1}$)	8.314
Molar Mass, M (kg/mol)	0.016
Gas density, ρ (kg/m^3)	15.19
Gas pressure, P (MPa)	3
Press gradient, ∇P (MPa/m)	-1
Dynamic viscosity, μ ($\text{kg} \cdot \text{m}^{-1} \cdot \text{s}^{-1}$)	1.4×10^{-5}

Table 2

Average porosity and Kn of the reconstructed intergranular pore structures.

Set (#)	1	2	3	4	5
ϕ , (%)	8	10	12	14	16
ϕ_e , (%)	4.28	7.69	11.34	13.67	15.72
Kn	0.59	0.55	0.52	0.49	0.46

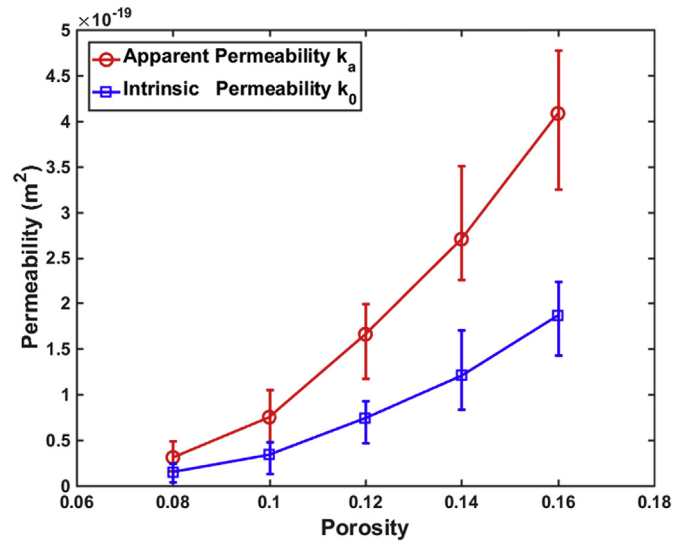


Fig. 6. Apparent permeability and intrinsic permeability of the intergranular pore model calculated by LBM simulations.

model has much larger k_0 and k_a , especially at small porosities. For instance, porosities of 8% or 10% yield permeabilities that are larger by more than one order of magnitude for the micro-cracks model. This can be related to a larger effective porosity and less complex pore morphology for the micro-crack model. This comparison implies the importance of pore morphology on gas permeability. Moreover, the highly permeable micro-crack models suggest that they play an important role in shale gas production.

4.3. Micro-gaseous flow in honeycomb pore model

Unlike the previous two inorganic pore models, the honeycomb pore model is a representation of the porous structure in organic matter. However, this work only focused on the influence of pore morphology on gas permeability, the influence of pore surface properties, such as the adsorbed gas layer on organic pores (Li et al., 2016; Ren et al., 2014; Sang et al., 2016), was not included in the current calculations. The ϕ_e and Kn of the ten structures in each porosity set are shown in Table 3. k_0 and k_a of the five sets of honeycomb pore model, which have a porosity ranging from 30% to 50%, were calculated using LBM.

Again, two series of LBM simulations, with and without considering the high- Kn effect, were performed to obtain k_a and k_0 . Results of k_a and k_0 are plotted against porosity in Fig. 8, in which k_a and k_0 increase with increasing porosity. Compared with the intergranular pore model, the honeycomb pore model has much larger permeability since its effective porosity and effective channel size is much larger. However, it should be noted that the permeabilities of the honeycomb pore model and micro-crack model were within the same order of magnitude although porosities were much larger for the honeycomb model. This again demonstrates the importance of pore morphology on transport properties within shales.

5. Conclusions

Our preliminary results show that the FIB-SEM method provides a useful tool to characterize different pore morphologies in a shale matrix. Based on the characterizations of the pore morphology,

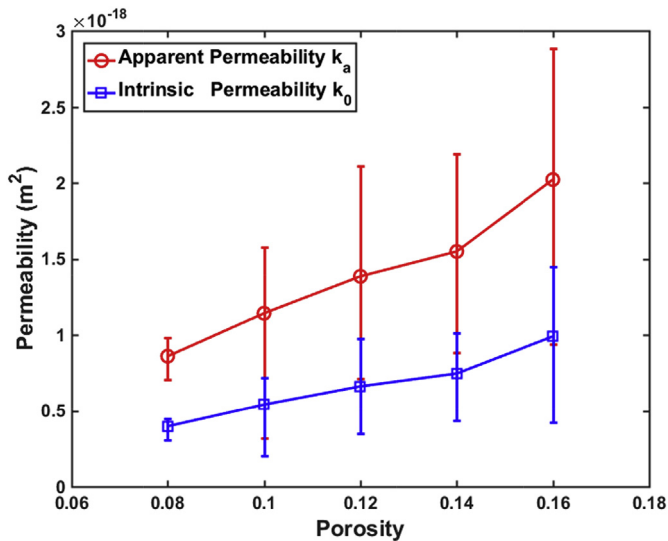


Fig. 7. Apparent permeability and intrinsic permeability of the micro-crack model calculated by LBM simulations.

Table 3
Average porosity and Kn of the reconstructed honeycomb pore structures.

Set (#)	1	2	3	4	5
ϕ (%)	30	35	40	45	50
ϕ_e (%)	25.20	32.72	39.35	44.59	49.79
Kn	0.25	0.24	0.22	0.22	0.20

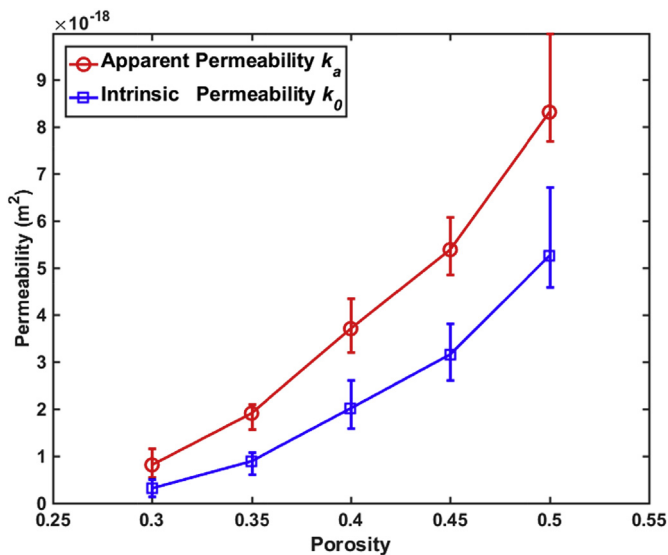


Fig. 8. Apparent permeability and intrinsic permeability of the generated honeycomb pore model calculated by LBM simulations.

three conceptual models with different pore morphologies were proposed: 1) the intergranular pore model, 2) the micro-crack model and 3) the honeycomb pore model. These conceptual models were then numerically generated for different porosity ranges. Finally, LBM with the MRT collision operator was employed to simulate the micro-gaseous flows in these reconstructed structures. A lower effective gas viscosity and a diffusive wall boundary condition were employed in the LBM to capture the high-Knudsen

effect in the nano-scale porous structures. As the calculation results showed, the permeability of the micro-crack model showed a positive linear correlation with increasing porosity. Besides, the permeability of the micro-crack model was much larger when compared to the intergranular pore model albeit the same porosity. Although the honeycomb pore model was generated with much larger porosities than micro-crack model, the permeabilities of these two models are in the same order of magnitude. These results numerically prove that micro-cracks have a major contribution to gas transport within a shale matrix. In addition, the apparent permeability within each model was about two times larger than the intrinsic permeability for each model. This emphasizes that the high-Knudsen effect must be considered when estimating shale gas production rates.

Acknowledgement

The authors are grateful to the National Natural Science Foundation of China (Grant No. 51374213, U1562217), the National Natural Science Funds for Distinguished Young Scholars of China (Grant No. 51125017), the State Key Research Development Program of China (Grant No. 2016YFC0600705), National Science and Technology Major Project on Oil and Gas (No.2017ZX05013001), PetroChina Innovation Foundation (No. 2015D-5006-0201) and the Science Fund for Creative Research Groups of the National Natural Science Foundation of China (Grant No. 51421003) for the financial supports. The authors would like to express their gratitude to Garri Gaus from RWTH Aachen University and the anonymous reviewers for their valuable suggestions and comments, which have greatly improved this paper.

References

- Aidun, C.K., Clausen, J.R., 2010. Lattice-Boltzmann method for complex flows. *Annu. Rev. Fluid Mech.* 42, 439–472.
- Akbarabadi, M., Piri, M., 2014. Nanotomography of the spontaneous imbibition in shale. In: *SPE/AAPG/SEG Unconventional Resources Technology Conference*. Society of Petroleum Engineers, Denver, Colorado, USA.
- Ansumali, S., Karlin, I.V., 2002. Kinetic boundary conditions in the lattice Boltzmann method. *Phys. Rev. E* 66, 026311.
- Bazant, Z.P., Salvati, M., Chau, V.T., Viswanathan, H., Zubelewicz, A., 2014. Why fracking works. *J. Appl. Mech.-T ASME* 81, 101010.
- Beskok, A., Karniadakis, G.E., 1999. A model for flows in channels, pipes, and ducts at micro and nano scales. *Nanoscale Microscale Thermophys. Eng.* 3, 43–77.
- Bultreys, T., De Boever, W., Cnudde, V., 2016. Imaging and image-based fluid transport modeling at the pore scale in geological materials: a practical introduction to the current state-of-the-art. *Earth-Science Rev.* 155, 93–128.
- Carman, P.C., 1997. Fluid flow through granular beds. *Chem. Eng. Res. Des.* 75, S32–S48.
- Chai, Z., Lu, J., Shi, B., Guo, Z., 2011. Gas slippage effect on the permeability of circular cylinders in a square array. *Int. J. Heat Mass Tran.* 54, 3009–3014.
- Chalmers, G.R., Bustin, R.M., Power, I.M., 2012. Characterization of gas shale pore systems by porosimetry, pycnometry, surface area, and field emission scanning electron microscopy/transmission electron microscopy image analyses: examples from the Barnett, Woodford, Haynesville, Marcellus, and Doig units. *AAPG Bull.* 96, 1099–1119.
- Chen, S., Gary, D.D., 1998. Lattice Boltzmann method for fluid flows. *Annu. Rev. Fluid Mech.* 30, 329–364.
- Cho, H., Jeong, N., Sung, H.J., 2013. Permeability of microscale fibrous porous media using the lattice Boltzmann method. *Int. J. Heat Fluid Flow* 44, 435–443.
- Civan, F., 2010. Effective correlation of apparent gas permeability in tight porous media. *Transp. Porous Med.* 82, 375–384.
- d’Humières, D., 2002. Multiple-relaxation-time lattice boltzmann models in three dimensions, philosophical transactions of the royal society of London. *Ser. A. Math. Phys. Eng. Sci.* 360, 437–451.
- Fink, R., Krooss, B.M., Gensterblum, Y., Amann-Hildenbrand, A., 2017. Apparent permeability of gas shales – superposition of fluid-dynamic and poro-elastic effects. *Fuel* 199, 532–550.
- Gensterblum, Y., Ghanizadeh, A., Cuss, R.J., Amann-Hildenbrand, A., Krooss, B.M., Clarkson, C.R., Harrington, J.F., Zoback, M.D., 2015. Gas transport and storage capacity in shale gas reservoirs – a review. Part A: transport processes. *J. Unconv. Oil Gas. Resour.* 12, 87–122.
- Guo, Z.L., Zheng, C.G., Shi, B.C., 2002. Non-equilibrium extrapolation method for velocity and pressure boundary conditions in the lattice boltzmann method. *Chin. Phys. (Overseas Ed.)* 11, 366–374.

- Guo, Z., Zheng, C., Shi, B., 2008. Lattice Boltzmann equation with multiple effective relaxation times for gaseous microscale flow. *Phys. Rev. E* 77, 036707.
- He, X., Luo, L.-S., 1997. Theory of the lattice Boltzmann method: from the Boltzmann equation to the lattice Boltzmann equation. *Phys. Rev. E* 56, 6811–6817.
- Heller, R., Vermynen, J., Zoback, M., 2014. Experimental investigation of matrix permeability of gas shales. *AAPG Bull.* 98, 975–995.
- Jackson, R.B., Vengosh, A., Carey, J.W., Davies, R.J., Darragh, T.H., O'Sullivan, F., Petron, G., 2014. The environmental costs and benefits of fracking. *Annu. Rev. Environ. Resour.* 39, 327–362.
- Javadpour, F., Fisher, D., Unsworth, M., 2007. Nanoscale gas flow in shale gas sediments. *J. Can. Petrol Technol.* 46, 55–61.
- Ju, Y., Yang, Y., Peng, R., Mao, L., 2013. Effects of pore structures on static mechanical properties of sandstone. *J. Geotechnical Geoenvironmental Eng.* 139, 1745–1755.
- Ju, Y., Zheng, J., Epstein, M., Sudak, L., Wang, J., Zhao, X., 2014. 3D numerical reconstruction of well-connected porous structure of rock using fractal algorithms. *Comput Method Appl. M.* 279, 212–226.
- Ju, Y., Gong, W., Chang, C., Xie, H., Xie, L., Liu, P., 2017. Three-dimensional characterisation of multi-scale structures of the Silurian Longmaxi shale using focused ion beam-scanning electron microscopy and reconstruction technology. *J. Nat. Gas. Sci. Eng.* 46, 26–37.
- Ju, Y., Huang, Y., Zheng, J., Qian, X., Xie, H., Zhao, X., 2017. Multi-thread parallel algorithm for reconstructing 3D large-scale porous structures. *Comput. Geosciences* 101, 10–20.
- Kalarakis, A.N., Michalis, V.K., Skouras, E.D., Burganos, V.N., 2012. Mesoscopic simulation of rarefied flow in narrow channels and porous media. *Transp. Porous Med.* 94, 385–398.
- Kelly, S., El-Sobky, H., Torres-Verdín, C., Balhoff, M.T., 2016. Assessing the utility of FIB-SEM images for shale digital rock physics. *Adv. Water Resour.* 95, 302–316.
- Klaver, J., Desbois, G., Littke, R., Urai, J.L., 2015. BIB-SEM characterization of pore space morphology and distribution in postmature to overmature samples from the Haynesville and Bossier Shales. *Mar. Petrol Geol.* 59, 451–466.
- Klinkenberg, L., 1941. *The Permeability of Porous Media to Liquids and Gases. Drilling and production practice*, New York, USA, pp. 200–213.
- Lauga, E., Brenner, M., Stone, H., 2007. *Microfluidics: the No-Slip boundary condition*. In: Tropea, C., Yarin, A.L., Foss, J.F. (Eds.), *Springer Handbook of Experimental Fluid Mechanics*. Springer Berlin Heidelberg, Berlin, Heidelberg, pp. 1219–1240.
- Li, Q., He, Y.L., Tang, G.H., Tao, W.Q., 2011. Lattice Boltzmann modeling of micro-channel flows in the transition flow regime. *Microfluid. Nanofluidics* 10, 607–618.
- Li, Z.-Z., Min, T., Kang, Q., He, Y.-L., Tao, W.-Q., 2016. Investigation of methane adsorption and its effect on gas transport in shale matrix through microscale and mesoscale simulations. *Int. J. Heat. Mass Tran* 98, 675–686.
- Liang, C., Jiang, Z., Zhang, C., Guo, L., Yang, Y., Li, J., 2014. The shale characteristics and shale gas exploration prospects of the lower Silurian Longmaxi shale, Sichuan Basin, South China. *J. Nat. Gas. Sci. Eng.* 21, 636–648.
- Loucks, R.G., Reed, R.M., Ruppel, S.C., Hammes, U., 2012. Spectrum of pore types and networks in mudrocks and a descriptive classification for matrix-related mudrock pores. *AAPG Bull.* 96, 1071–1098.
- Ohwada, T., Sone, Y., Aoki, K., 1989. Numerical analysis of the shear and thermal creep flows of a rarefied gas over a plane wall on the basis of the linearized Boltzmann equation for hard-sphere molecules. *Phys. Fluids A: Fluid Dyn.* 1, 1588–1599.
- Pan, C., Luo, L.-S., Miller, C.T., 2006. An evaluation of lattice Boltzmann schemes for porous medium flow simulation. *Comput Fluids* 35, 898–909.
- Ren, J., Guo, P., Guo, Z., Wang, Z., 2014. A lattice Boltzmann model for simulating gas flow in kerogen pores. *Transp. Porous Med.* 106, 285–301.
- Sang, Q., Li, Y., Yang, Z., Zhu, C., Yao, J., Dong, M., 2016. Experimental investigation of gas production processes in shale. *Int. J. Coal Geol.* 159, 30–47.
- Suga, K., Takenaka, S., Ito, T., Kaneda, M., Kinjo, T., Hyodo, S., 2010. Evaluation of a lattice Boltzmann method in a complex nanoflow. *Phys. Rev. E* 82, 016701.
- Sukop, M.C., Thorne, D.T.J., 2006. *Lattice Boltzmann Modeling: an Introduction for Geoscientists and Engineers*. Springer, New York.
- Wang, M., Li, Z.X., 2003. Nonideal gas flow and heat transfer in micro- and nano-channels using the direct simulation Monte Carlo method. *Phys. Rev. E* 68.
- Wang, M., Pan, N., 2008. Predictions of effective physical properties of complex multiphase materials. *Mater. Sci. Eng. R: Rep.* 63, 1–30.
- Wang, L., Yin, X., 2017. Apparent permeability of flow through periodic arrays of spheres with first-order slip. *Powder Technol.* 311, 313–327.
- Wang, M., Lan, X.D., Li, Z.X., 2008. Analyses of gas flows in micro- and nano-channels. *Int. J. Heat Mass Transf.* 51, 3630–3641.
- Wang, M., Kang, Q., Viswanathan, H., Robinson, B.A., 2010. Modeling of electroosmosis of dilute electrolyte solutions in silica microporous media. *J. Geophys. Res. Sol. Ea.* 115, 10201–10209. B10205.
- Wang, Z., Jin, X., Wang, X., Sun, L., Wang, M., 2016. Pore-scale geometry effects on gas permeability in shale. *J. Nat. Gas. Sci. Eng.* 34, 948–957.
- Wang, Z., Guo, Y., Wang, M., 2016. Permeability of high-Kn real gas flow in shale and production prediction by pore-scale modeling. *J. Nat. Gas. Sci. Eng.* 28, 328–337.
- Wang, J., Chen, L., Kang, Q., Rahman, S.S., 2016. The lattice Boltzmann method for isothermal micro-gaseous flow and its application in shale gas flow: a review. *Int. J. Heat. Mass Tran* 95, 94–108.
- Wu, L., Struchtrup, H., 2017. Assessment and development of the gas kinetic boundary condition for the Boltzmann equation. *J. Fluid Mech.* 823, 511–537.
- Zheng, J., Ju, Y., Liu, H.-H., Zheng, L., Wang, M., 2016. Numerical prediction of the decline of the shale gas production rate with considering the geomechanical effects based on the two-part Hooke's model. *Fuel* 185, 362–369.